

MICROCOPY RESOLUTION TEST CHART
NATIONAL BUREAU OF STANDARDS-1963-A

AD-A174 499



ON THE MODELING OF A LARGE-SCALE ELECTRO-OPTIC SYSTEM

Stephen John Walsh

July 1986

Final Report

Approved for public release; distribution unlimited.

DTIC
ELECTE
NOV 26 1986

S

D

B

AIR FORCE WEAPONS LABORATORY
Air Force Systems Command
Kirtland Air Force Base, NM 87117-6008

DTIC FILE COPY

This final report was prepared by the Air Force Weapons Laboratory, Kirtland Air Force Base, Albuquerque, New Mexico, Job Order 317J1D01. Richard A. Carreras (ARBB) was the Laboratory Project Officer-in-Charge.

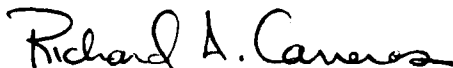
When Government drawings, specifications, or other data are used for any purpose other than in connection with a definitely Government-related procurement, the United States Government incurs no responsibility or any obligation whatsoever. The fact that the Government may have formulated or in any way supplied the said drawings, specifications, or other data, is not to be regarded by implication, or otherwise in any manner construed, as licensing the holder, or any other person or corporation; or conveying any rights or permission to manufacture, use, or sell any patented invention that may in any way be related thereto.

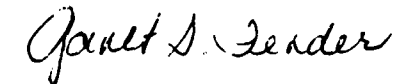
This report has been authored by an employee of the United States Government. Accordingly, the United States Government retains a nonexclusive, royalty-free license to publish or reproduce the material contained herein, or allow others to do so, for the United States Government purposes.

This report has been reviewed by the Public Affairs Office and is releasable to the National Technical Information Service (NTIS). At NTIS, it will be available to the general public, including foreign nations.

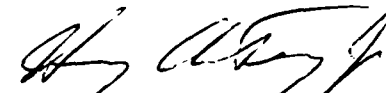
If your address has changed, if you wish to be removed from our mailing list, or if your organization no longer employs the addressee, please notify AFWL/ARBB, Kirtland AFB, NM 87117-6008 to help us maintain a current mailing list.

This technical report has been reviewed and is approved for publication.


RICHARD A. CARRERAS
Project Officer


JANET S. FENDER
Chief, Phased Array Branch

FOR THE COMMANDER


HARRY A. TRACY
Maj, USAF
Chief, Optics and Beam Control Division

DO NOT RETURN COPIES OF THIS REPORT UNLESS CONTRACTUAL OBLIGATIONS OR NOTICE ON A SPECIFIC DOCUMENT REQUIRES THAT IT BE RETURNED.

UNCLASSIFIED

SECURITY CLASSIFICATION OF THIS PAGE

ADA 174499

REPORT DOCUMENTATION PAGE

1a. REPORT SECURITY CLASSIFICATION Unclassified			1b. RESTRICTIVE MARKINGS		
2a. SECURITY CLASSIFICATION AUTHORITY			3. DISTRIBUTION / AVAILABILITY OF REPORT Approved for public release; distribution unlimited.		
2b. DECLASSIFICATION / DOWNGRADING SCHEDULE			5. MONITORING ORGANIZATION REPORT NUMBER(S)		
4. PERFORMING ORGANIZATION REPORT NUMBER(S) AFWL-TR-86-34			7a. NAME OF MONITORING ORGANIZATION		
6a. NAME OF PERFORMING ORGANIZATION Air Force Weapons Laboratory		6b. OFFICE SYMBOL (If applicable)		7b. ADDRESS (City, State, and ZIP Code)	
6c. ADDRESS (City, State, and ZIP Code) Kirtland AFB, NM 87117-6008			9. PROCUREMENT INSTRUMENT IDENTIFICATION NUMBER		
8a. NAME OF FUNDING / SPONSORING ORGANIZATION		8b. OFFICE SYMBOL (If applicable)		10. SOURCE OF FUNDING NUMBERS	
8c. ADDRESS (City, State, and ZIP Code)		PROGRAM ELEMENT NO. 63221C		PROJECT NO. 317J	TASK NO. 1D
				WORK UNIT ACCESSION NO. 01	
11. TITLE (Include Security Classification) ON THE MODELING OF A LARGE-SCALE ELECTRO-OPTIC SYSTEM					
12. PERSONAL AUTHOR(S) Walsh, Stephen John					
13a. TYPE OF REPORT Final		13b. TIME COVERED FROM Jan 85 TO Apr 86		14. DATE OF REPORT (Year, Month, Day) 1986 July	
				15. PAGE COUNT 60	
16. SUPPLEMENTARY NOTATION					
17. COSATI CODES			18. SUBJECT TERMS (Continue on reverse if necessary and identify by block number)		
FIELD	GROUP	SUB-GROUP	synthetic aperture		
20	06		multiple aperture		
20	05		control system modeling		
19. ABSTRACT (Continue on reverse if necessary and identify by block number) Through this examination of a three-aperture bench laser experiment, a large-scale system realization model has been obtained. This realization model represents a valuable investigative tool for further control analysis and phased array experimental research. The experimental system was decomposed into five weakly coupled control loops that contained six components each. Transfer-function matrices for individual components were obtained through analysis of electrical schematics, experimental Bode plots, and through existing empirical data. The component models were cascaded together to form forward-loop transfer-function matrices for the five control loops. Closed-loop transfer-function matrices in observable canonical form were subsequently obtained. The modal matrices corresponding to three of the control loops were so poorly conditioned that a decoupled composite dynamical equation-based realization of high order was necessitated. The remaining two closed-loop transfer-function matrices were realized by solving a 14th order (over)					
20. DISTRIBUTION / AVAILABILITY OF ABSTRACT <input checked="" type="checkbox"/> UNCLASSIFIED/UNLIMITED <input type="checkbox"/> SAME AS RPT <input type="checkbox"/> DTIC USERS			21. ABSTRACT SECURITY CLASSIFICATION Unclassified		
22a. NAME OF RESPONSIBLE INDIVIDUAL Richard A. Carreras			22b. TELEPHONE (Include Area Code) (505) 846-3694		22c. OFFICE SYMBOL ARBB

19. ABSTRACT (Continued)

differential equation for the highest derivative term. This equation was then transformed into a nested sequence of integrations, and the state differential equations were obtained via a simulation diagram. This procedure led to irreducible, observable canonical form realizations.

The 208th order, three-aperture model retains the potential for complete coupling, although all experimental data indicate that the large-scale system is weakly coupled. This further strengthens the model's utility.

Pages 20 and 21 do not contain proprietary information.

Per Mrs. Margaret Nieto, AFWL/SUR

Accession For	
NTIS GRA&I	<input checked="" type="checkbox"/>
DTIC TAB	<input type="checkbox"/>
Unannounced	<input type="checkbox"/>
Justification	
By	
Distribution/	
Availability Codes	
Dist	Avail and/or Special
A-1	



TABLE OF CONTENTS

CHAPTER 1	Introduction	1
CHAPTER 2	Modeling	5
	2.1 Tilt Loop	5
	2.1.1 Compensator	5
	2.1.2 Axis Separator	7
	2.1.3 High Voltage Amplifier	11
	2.1.4 Actuator	13
	2.1.5 Tilt Optics	15
	2.1.6 Quadrant Cell and UDT 431	18
	2.2 Piston Loop	25
	2.2.1 Compensator	25
	2.2.2 Axis Separator	25
	2.2.3 Piston Optics	26
	2.2.4 Phase Management Data Processor	26
	2.3 Tilt-Piston Coupling	31
CHAPTER 3	Realization	33
	3.1 Tilt Loop	33
	3.2 Piston Loop	38
	3.3 Stability	38
	3.4 Large-Scale System	42
CHAPTER 4	Conclusions	46
APPENDIX	Glossary of Abbreviations	50
REFERENCES	51

LIST OF FIGURES

Figure		
1	Experimental Layout of PHASAR System . . .	2
2	Component Block Control Diagram	4
3	Tilt Loop Block Diagram	5
4	Compensator Schematic	6
5	Notch Filter Schematic	8
6	Notch Filter Component Model Bode Plot . .	9
7	Coordinate Misalignment Axis	10
8	PZT Placement on Actuator	11
9	Typical HVA Bode Plot	12
10	OPDA Bode Plot	14
11	OPDA Component Model Bode Plot	16
12	Tilt Optics Layout	15
13	OPDA Geometry	17
14	Tilt Optics OPDA Triangle	17
15	Quad Cell Cross Section	18
16	UDT Schematic	20
17	Quad Cell Gain Geometry	23
18	Piston Loop Block Diagram	25
19	Displacement to OPD Translation	27
20	Interferogram Imaged onto LSC	29
21	Experimental Results	30
22	Simulated Algorithm Results	30

Figure

23	PMDP Gain	32
24	FLTF Tilt Loop	34
25	CLTF Tilt Loop	35
26	Tilt Loop Realization	36
27	FLTF Piston Loop	39
28	CLTF Piston Loop	39
29	Piston Loop Realization Procedure	40
30	Piston Loop Realization	41
31	Tilt FLTF Pole-Plot	43
32	Tilt CLTF Pole-Plot	45
33	Large-Scale System Realization	47

LIST OF TABLES

Table

1	Tilt FLTF Poles	44
2	Tilt CLTF Matrix Poles	46

CHAPTER 1

INTRODUCTION

The idea of constructing a very large optical aperture by combining several smaller, independent optical systems is a relatively new one to the optics community. Although this synthesis is standard for radar systems, the precision required to phase optical wavelengths posed a seemingly unattainable requirement. Recent demands for very large telescopes to advance astronomical frontiers and to perform defense missions have inspired innovative solutions to this problem. Within the past few years, the idea of aperture synthesis has established itself as the most promising technique for constructing mammoth optical systems.

Optical phasing of synthetic aperture systems require that each separate aperture have the same optical characteristics with regard to far field pattern and optical path length.⁹ In order to phase multiple telescopes together one must ensure that the wavefronts, as they are leaving their respective telescopes, are absolutely phased with respect to one another. They must also be kept pointing to the same spot in the optical far field. The Phased Array (PHASAR) Experiment is one such effort and is an on-going experiment at the Air Force Weapons Laboratory, Kirtland AFB, New Mexico.^{5,20} Figure 1 illustrates the experimental layout of the PHASAR system.

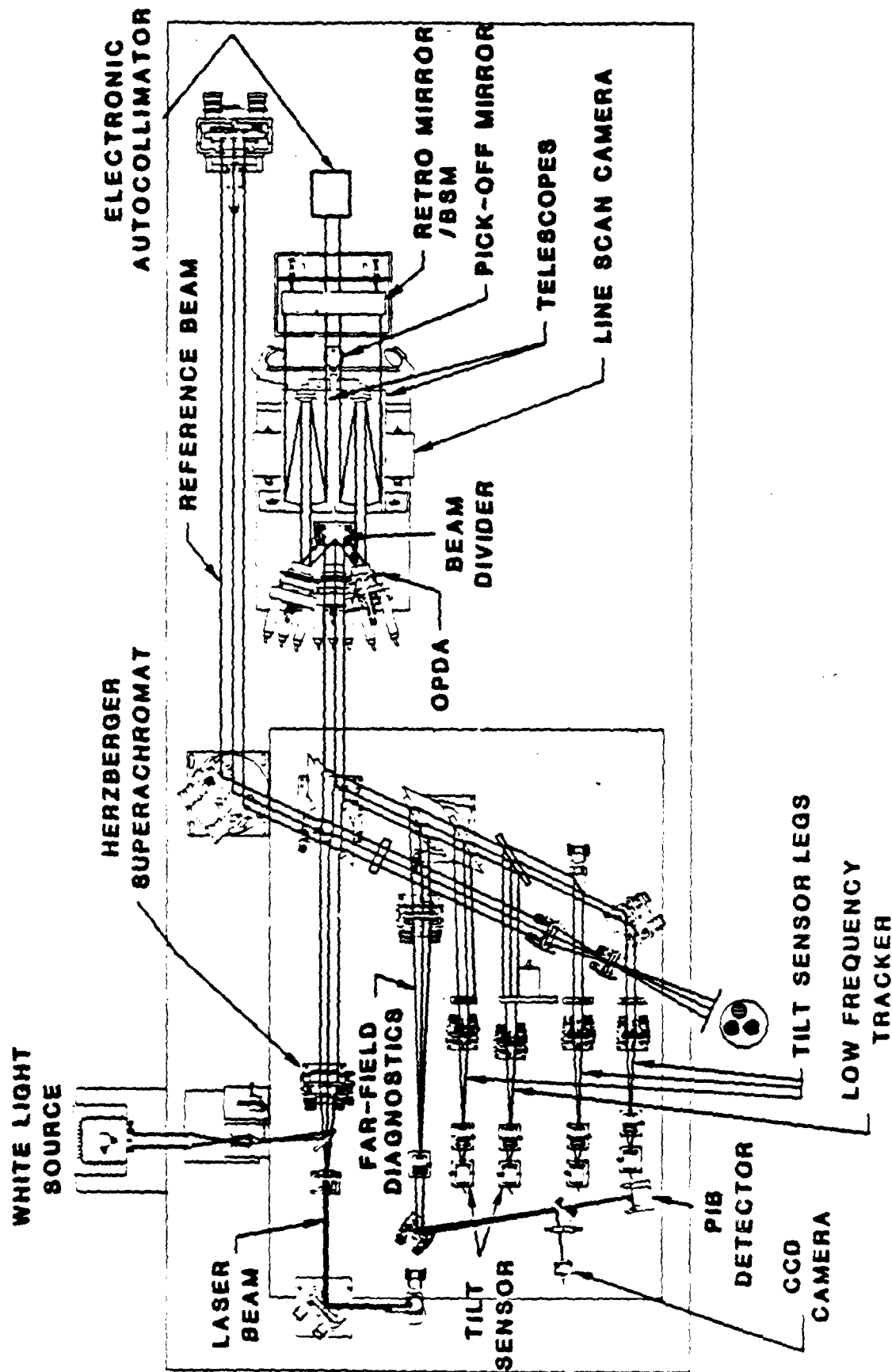


Figure 1. Experimental Layout of PHASAR System.

This experiment consists of three telescopes mounted within a single housing. Each telescope has a dedicated set of optical path difference adjusters. These adjusters steer a flat mirror so that each adjuster is capable of changing the optical path length, tilt error, and phase error of its respective telescope. These adjusters must be coordinated in a common reference system so that continuous phasing can be achieved. A number of electrical, optical, and electro-optical devices are being utilized to address these control issues. Peripheral control issues include open-loop control of the adjusters to allow for phasing of the telescopes while one or more apertures are moved in piston, and global determination of the point where there is no optical path difference between apertures.

Figure 2 shows the component block control diagram.

This project is being performed within prescribed limits determined by the thesis committee and the experimenters. Firstmost, the experimental optics are considered to be ideal by the models considered here. These optics have been previously modeled by and are well documented in PHASAR technical memorandums, so here the focus of the effort is toward the remainder of the experiment. Additionally, the tracker leg of this experiment has been excluded from modeling.

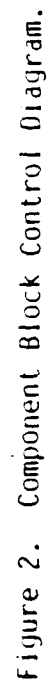


Figure 2. Component Block Control Diagram.

CHAPTER 2

MODELING

Referring again to Figure 2 we see that the block diagram is composed of two types of control loops: Tilt and Piston. This chapter outlines the modeling process for these loops in two major subsections.

2.1 TILT LOOP

The tilt loop was modeled with six components as shown in Figure 3. The two inputs and two outputs model the X and Y positions of the beam centroid striking the quad cell. There are three tilt loops in the system, one controlling each aperture in tilt.

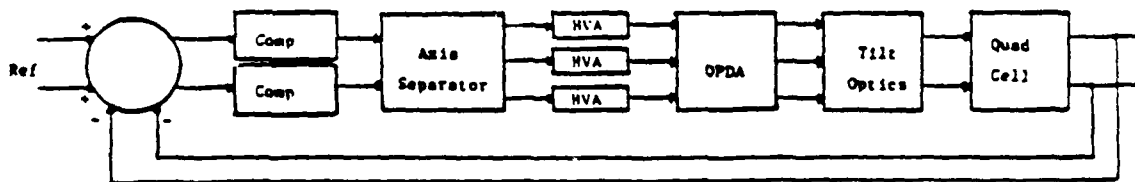


Figure 3. Tilt Loop Block Diagram.

2.1.1 COMPENSATOR

The compensator was built by the experimenters in order to operate the tilt error control loops within a desired bandwidth. A schematic of the compensator is shown in Figure 4. The companion

notch filter was inserted at the point marked A. It is shown in Figure 5. The compensator can be manually switched from a low pass filter to an integrator. It is normally operated as an integrator in closed-loop and as a low pass filter during open-loop. The component transfer functions were modeled after these schematics.¹⁹ Figure 6 contains a Bode plot of this component model.

$$\text{Integrator TF} : \frac{s^4 + 1.5708e1s^3 + 1.2337e2s^2 + 1.0465e3s + 4.4382e3}{s^5 + 3.2673e1s^4 + 4.0012e2s^3 + 2.1767e3s^2 + 4.4382e3s}$$

$$\text{Low pass TF} : \frac{s^4 + 1.5708e1s^3 + 1.2337e2s^2 + 1.0465e3s + 4.4382e3}{(1 + 5.305e-3s)(s^4 + 3.2673e1s^3 + 4.0012e2s^2 + 2.1767e3s + 4.4382e3)}$$

2.1.2 AXIS SEPARATOR

The axis separator is used to transform the signals which command the Optical Path Difference Adjustor (OPDA), to induce x-tilt, y-tilt and piston corrections to the apertures. The axis separator is implemented in various places via hardware summers and gain pots. The reason for the axis separator is that misalignment errors, the imperfect positioning of the Piezo-Electric Transducers (PZTs) on the OPDAs and the coupling between the PZTs represent errors that necessitate some means of minimization.

Misalignment errors are the results of not having the x-y coordinate frame of the quad cell oriented identically to the corresponding coordinate frame of the OPDA. Figure 7 illustrates this point.

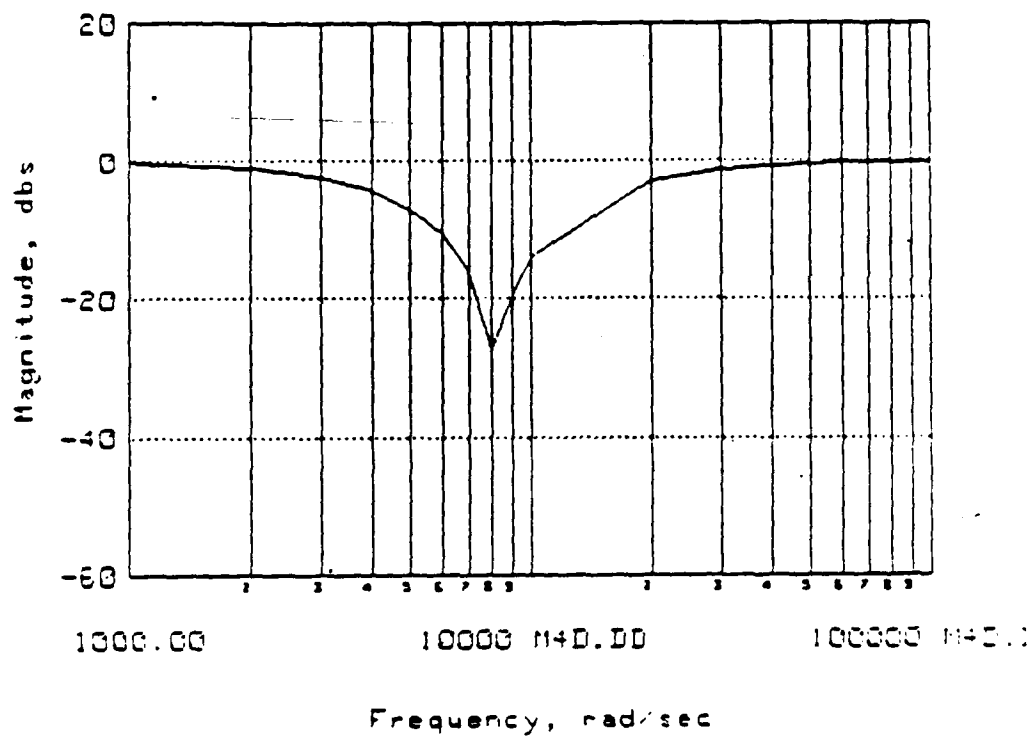


Figure 6. Notch Filter Component Model Bode Plot.

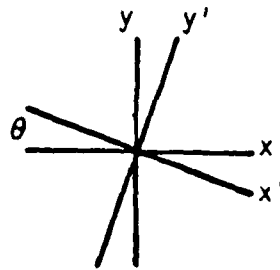


Figure 7. Coordinate Misalignment Axis.

The axis separator can be heuristically seen as compensating for the misalignment angle by modifying the movement commands sent to the PZTs. A simple direction cosine matrix will perform this function. With this misalignment angle nominally very small, the sine terms are at least two orders of magnitude less than the cosine terms.

$$\begin{bmatrix} x \\ y \end{bmatrix}_{\text{quad}} = \begin{bmatrix} \cos \theta & \sin \theta \\ -\sin \theta & \cos \theta \end{bmatrix} \begin{bmatrix} x \\ y \end{bmatrix}_{\text{OPDA}}$$

The positioning of the PZTs on the OPDAs is the major reason for the axis separator. It must transform commands in terms of x and y into individual commands to the three PZTs, d1, d2 and d3, as shown in Figure 8.

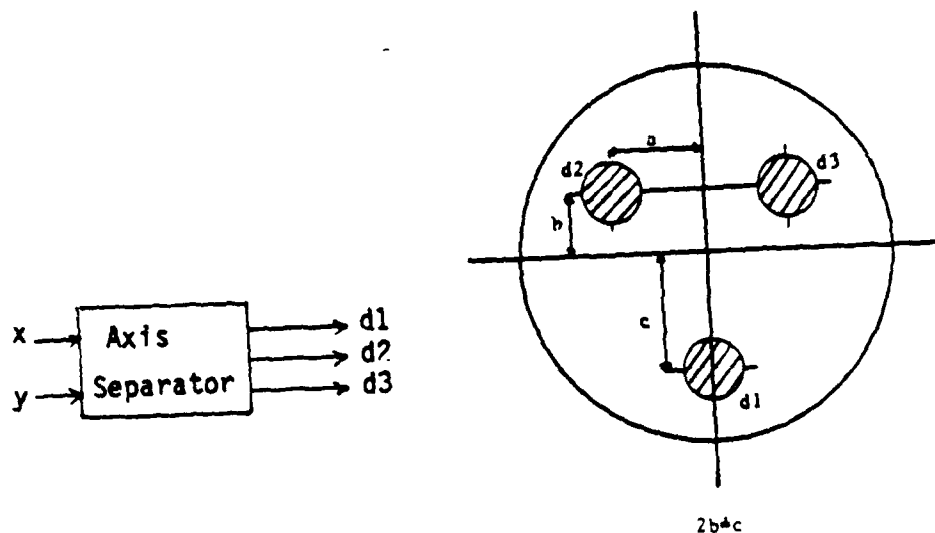


Figure 8.

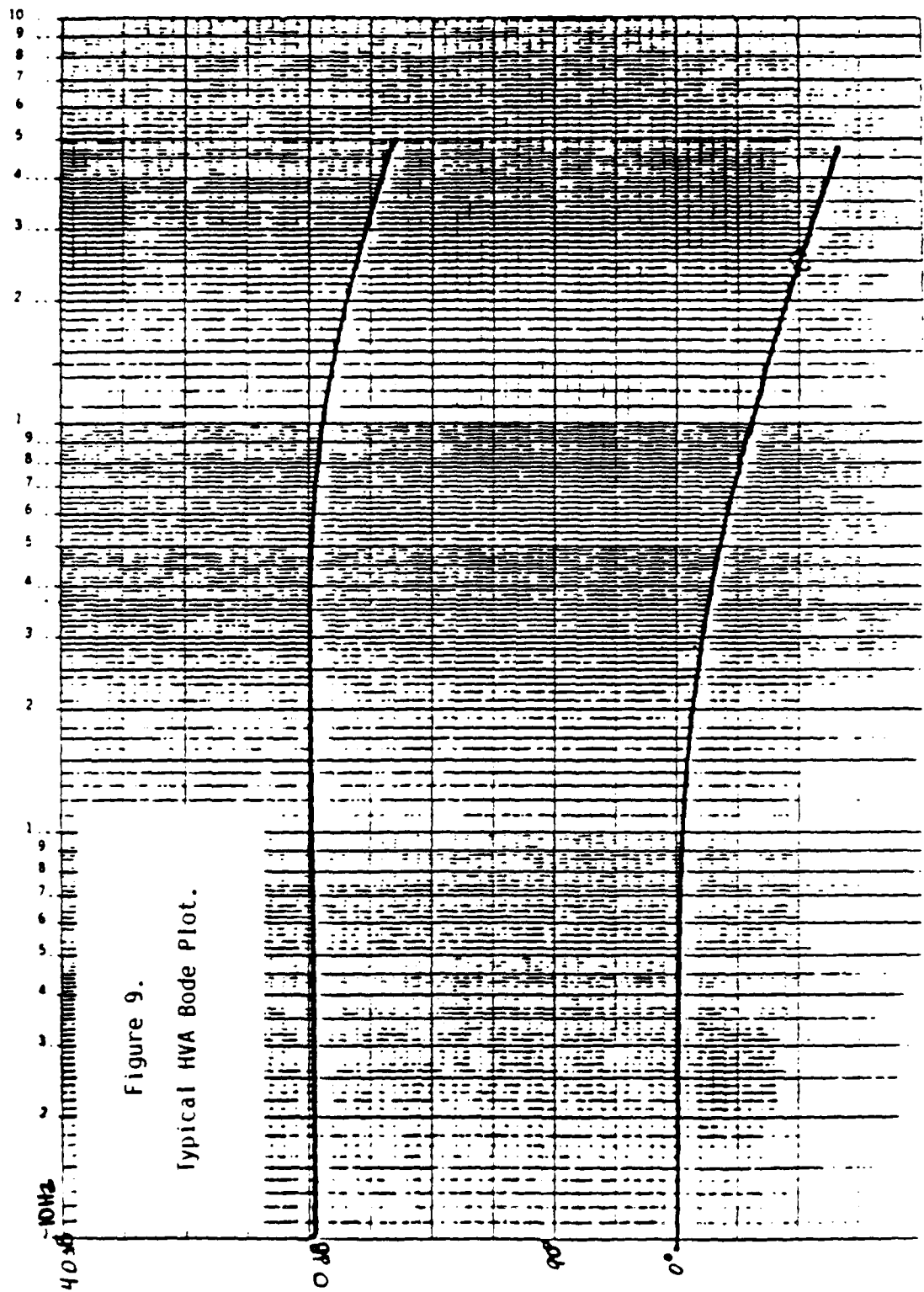
PZT Placement on Actuator.

A simple translation matrix performs this function. Here the gain is set at 2.5.

$$\begin{bmatrix} d1 \\ d2 \\ d3 \end{bmatrix} = 2.5 \begin{bmatrix} 0.0 & -1.0 \\ -1.0 & 0.5 \\ 1.0 & 0.5 \end{bmatrix} \begin{bmatrix} \cos \theta & \sin \theta \\ -\sin \theta & \cos \theta \end{bmatrix} \begin{bmatrix} x \\ y \end{bmatrix}$$

2.1.3 HIGH VOLTAGE AMPLIFIER

The high voltage amplifier (HVA) has a single stage gain of 200 and was custom built for this experiment by Los Alamos National Laboratory. They are used to amplify the signal sent to the PZTs in the OPDAs. Figure 9 represents a Bode plot of a typical HVA. The main features in this figure are the uniform rolloff of 24db per decade and zero phase lag. Taking the average of the plots from the



12 different HVAs, the corner frequency was calculated to be 1.458 KHz. The single pole model with the given corner frequency proved more accurate than a second order model that was heavily damped. So the transfer function for this component was chosen as:

$$\frac{200}{1 + 1.0916e-4s}$$

2.1.4 ACTUATOR

The optical path difference adjusters (OPDA), or actuators, were built for this experiment by the Rocketdyne Division of Rockwell International. The actuator is a dynamic flat mirror that can be positioned with great precision. Three PZTs are housed in a flexure that forms a mount for the mirror.¹³ When a PZT is actuated, it physically pushes against the back of the mirror, moving it in tilt or translating it in piston. If all three PZTs are actuated equally, the mirror translates in piston with little tilt movement. Since the PZT has a dynamic range of only five microns, motorized micrometers were stacked on the rear of each PZT to provide coarse adjustment in open loop operation. A Bode plot was drawn for the actuator and is shown in Figure 10. The dominant features of this plot are the 134 db per decade rolloff and the resonant behavior in the vicinity of 2.7 KHz. The OPDA was visibly vibrating near this frequency. The gain magnitude must be discounted because it was adjusted so as to fit within the physical limits of the plotting equipment. The model excludes the resonant behavior because it lies well outside the

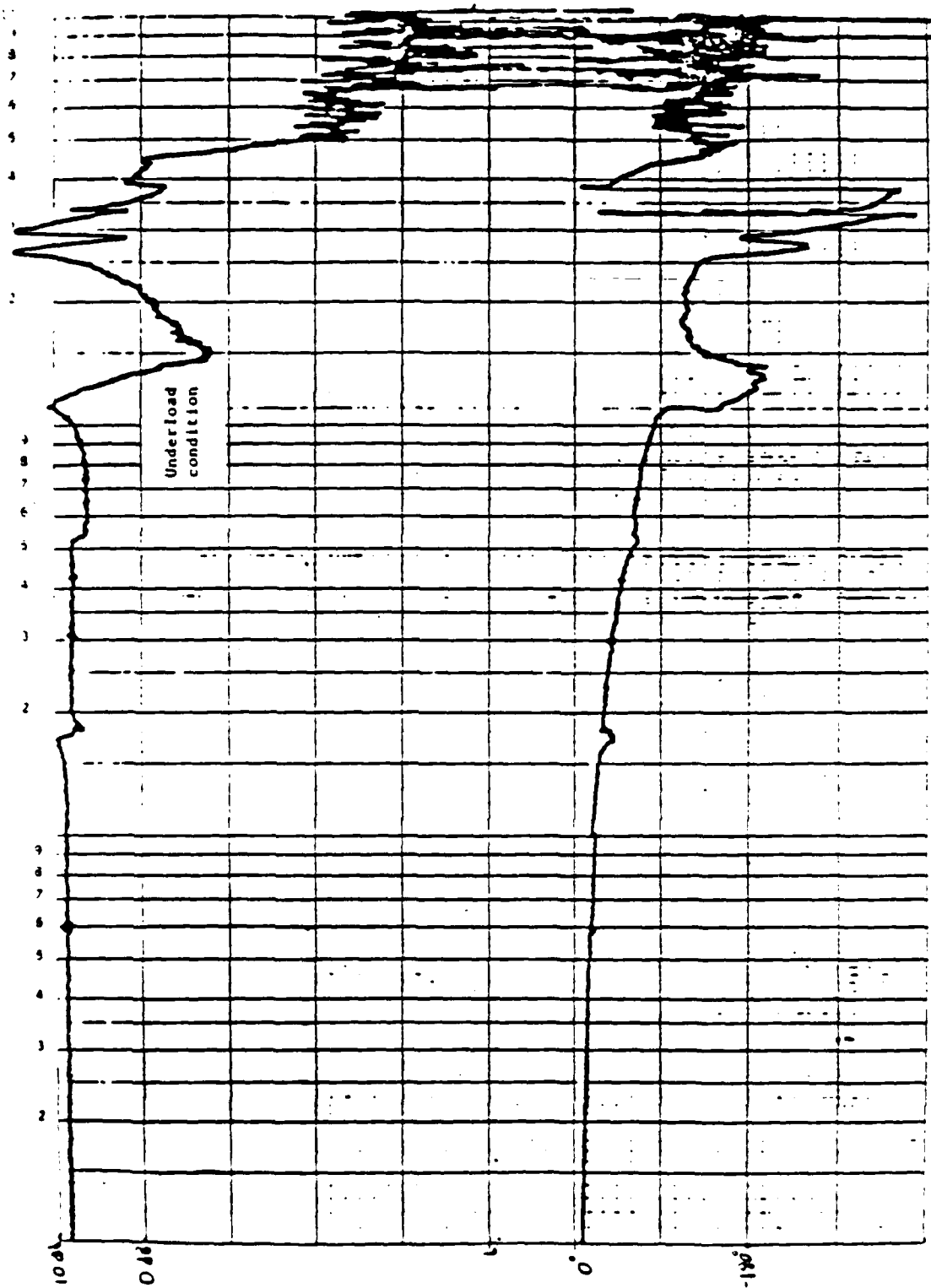


Figure 10. ORDA Bode Plot.

Figure 10.

bandwidth of the present experiment. After many discarded attempts, a seventh-order model was developed to represent this behavior. A Bode plot of its transfer function is shown in Figure 11. The gain of this transfer function corresponds to the plus or minus 500 volts from the HVA translating to a range of plus or minus 2.5 microns. So the transfer function for this component is:

$$\frac{5.0e-9}{(1+1.4469e-4s)(1+2.0256e-4s+2.0934e-8s^2)(1+6.8209e-5s+1.2924e-8s^2)^2}$$

2.1.5 TILT OPTICS

In this experiment quad cells are used to determine jitter and to aid in tracking.⁴ Their configurations are similar in that they all have a lens, and then a microscopic objective to reimage the beam onto the detector surface. Figure 12 illustrates a simplified layout.

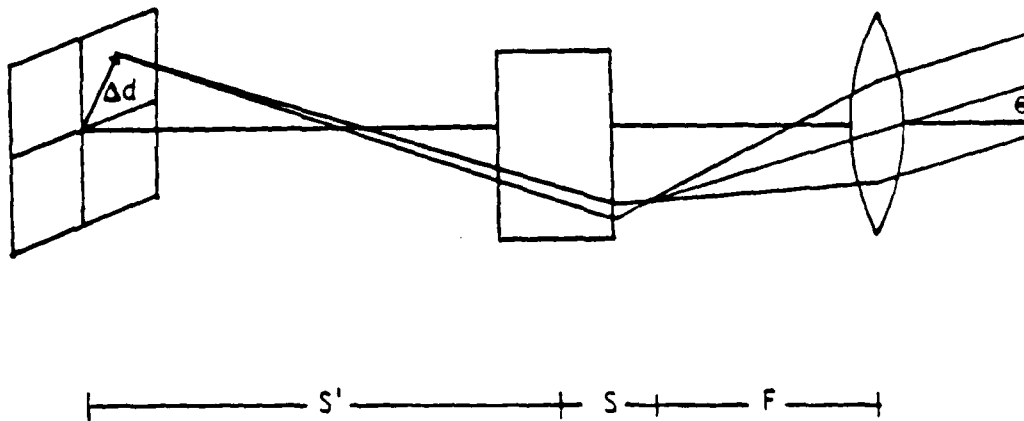


Figure 12. Tilt Optics Layout.

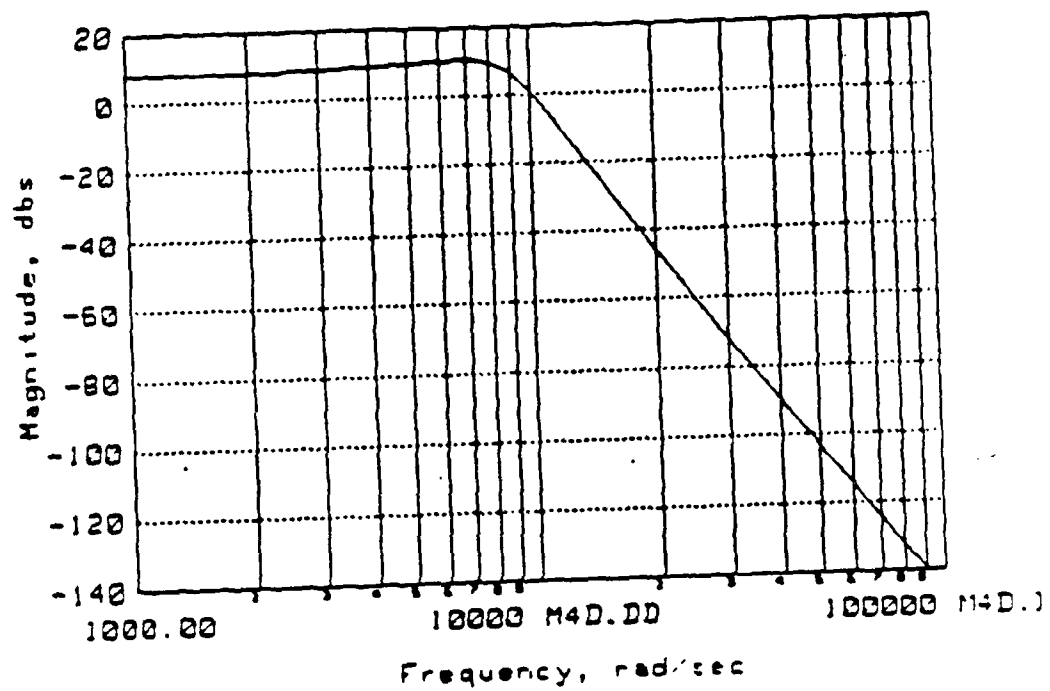


Figure 11. OPDA Component Model Bode Plot.

The x or y displacement of the quad cell is a function of the angle θ and the attributes of the optical setup. Here, $M = S'/S = 40.0$, and $F = 0.3$ meters. Then the displacement $\Delta d = F\theta M$ or $\Delta d = 12\theta$. An expression for θ was developed from the geometries of the actuator shown in Figure 13.

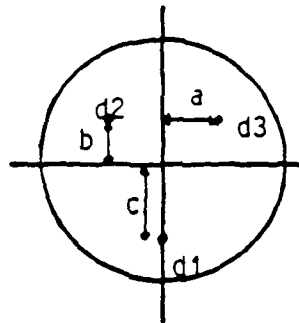


Figure 13. OPDA Geometry.

To determine Δx a right triangle is formed by the distance a , which was determined to be 0.01386 meters, and the commanded displacement. This triangle is shown in Figure 14.

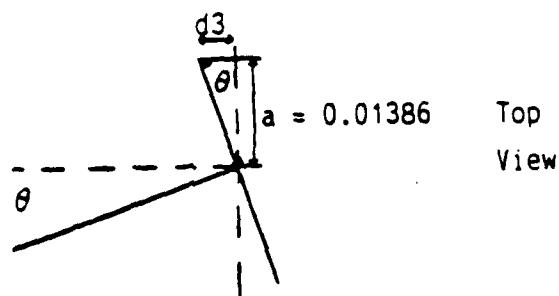


Figure 14. Tilt Optics OPDA Triangle.

Here, $\theta = \arctan(d3/a)$, and hence $\Delta x = 12 \arctan(d3/a)$. Similarly, we have $\Delta y = 12 \arctan(-d1/c)$. Since the \arctan function in this range can be linearized²² to $\arctan(k) = k$, our component transfer functions are:

$$\begin{bmatrix} x \\ y \end{bmatrix} = \begin{bmatrix} 0 & 0 & 865.8 \\ -750.0 & 0 & 0 \end{bmatrix} \begin{bmatrix} d1 \\ d2 \\ d3 \end{bmatrix}$$

2.1.6 QUADRANT CELL AND UDT 431

The quad cell is used to determine the displacement of the beam centroid striking its surface from the coordinate origin. The detector used in this experiment is a UDT Spot/40, position sensing photo detector quadrant cell. See Figure 15.

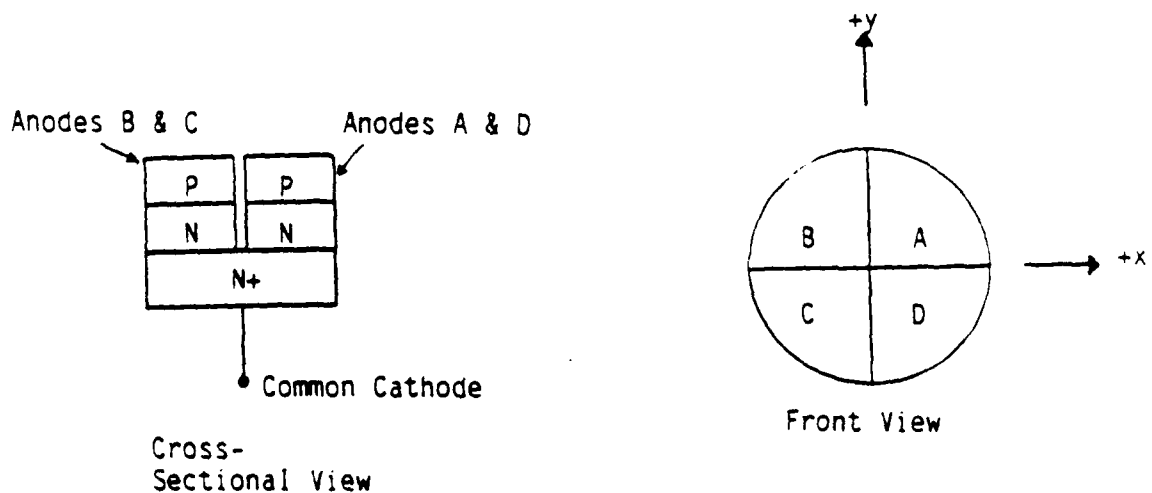


Figure 15. Quad Cell Cross Section.

The quad cell sensor has a bandwidth of 1 MHz and is therefore far outside the observed closed-loop system bandwidth of around 1 KHz. The UDT 431 X-Y position monitor is a processing unit that has the individual signals A, B, C and D as inputs the X and Y displacements along with other information not presently used in this experiment as outputs. The position equations for this detector use A, B, C and D to represent electrical terminal signal outputs. The equations are:

$$\text{X displacement: } x = \frac{(A + D) - (B + C)}{(A + B + C + D)}$$

$$\text{Y displacement: } y = \frac{(A + B) - (C + D)}{(A + B + C + D)}$$

From existing test data on the UDT 431, it was found that the X and Y displacement outputs have a bandwidth of about 1 KHz. This is caused by stages A21 and A25 driving both the position output as well as an analog meter. This limits bandwidth due to the high open-loop output impedance of the operational amplifier driving a 788 ohm meter as well as the output load. This low value of load resistance reduces the open-loop operational amplifier gain and as a result limits the bandwidth potential of the gain of 10 (open-loop) output driver (see Figure 16). This test data also verified that the analog divide module output was slew rate limited to 1.6 KHz. The gain would be a function of the signal processing if it were not for the analog divide stage normalizing the output. So then using the X and Y displacement

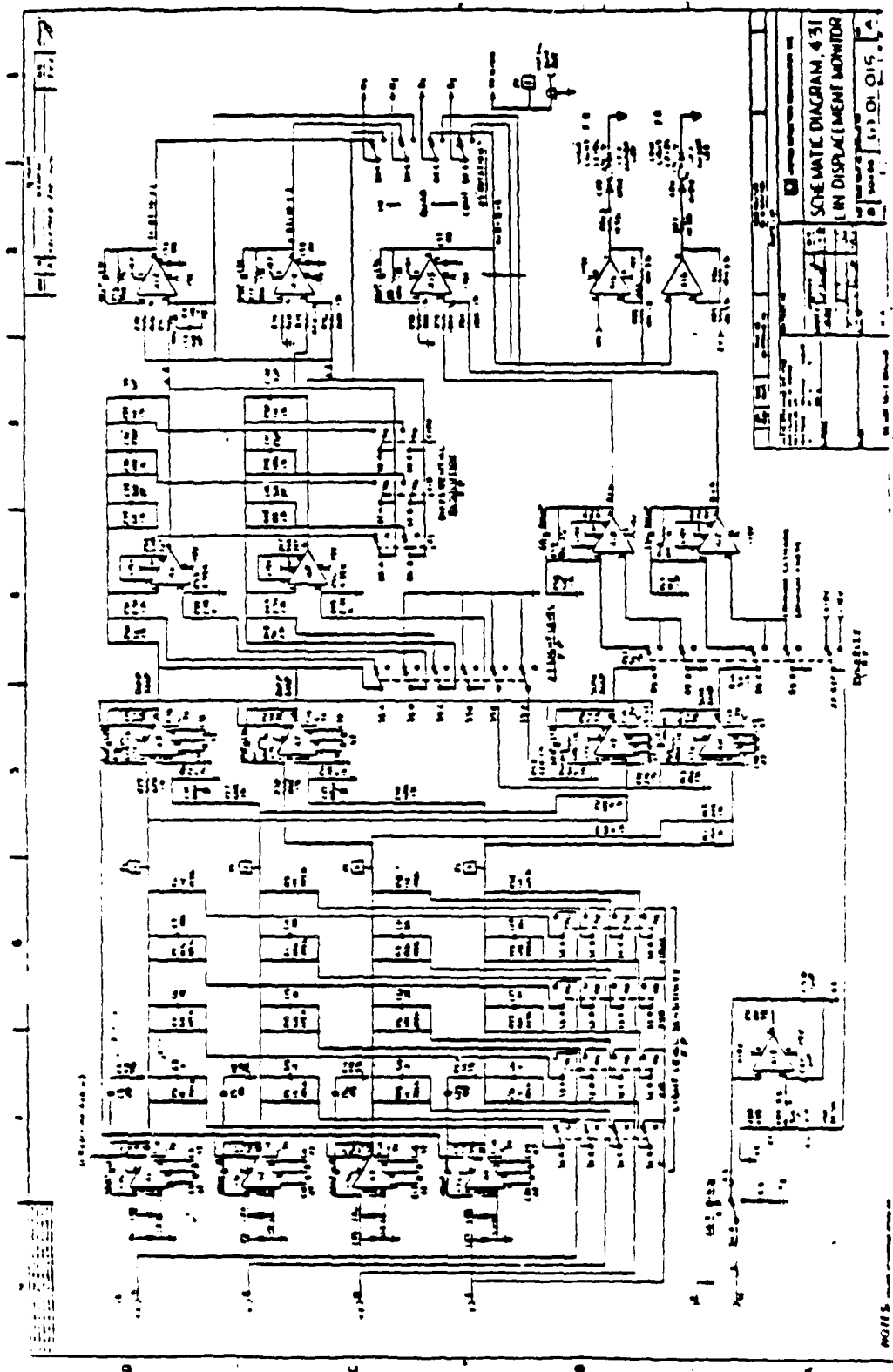


Figure 16a. UDI Schematic.

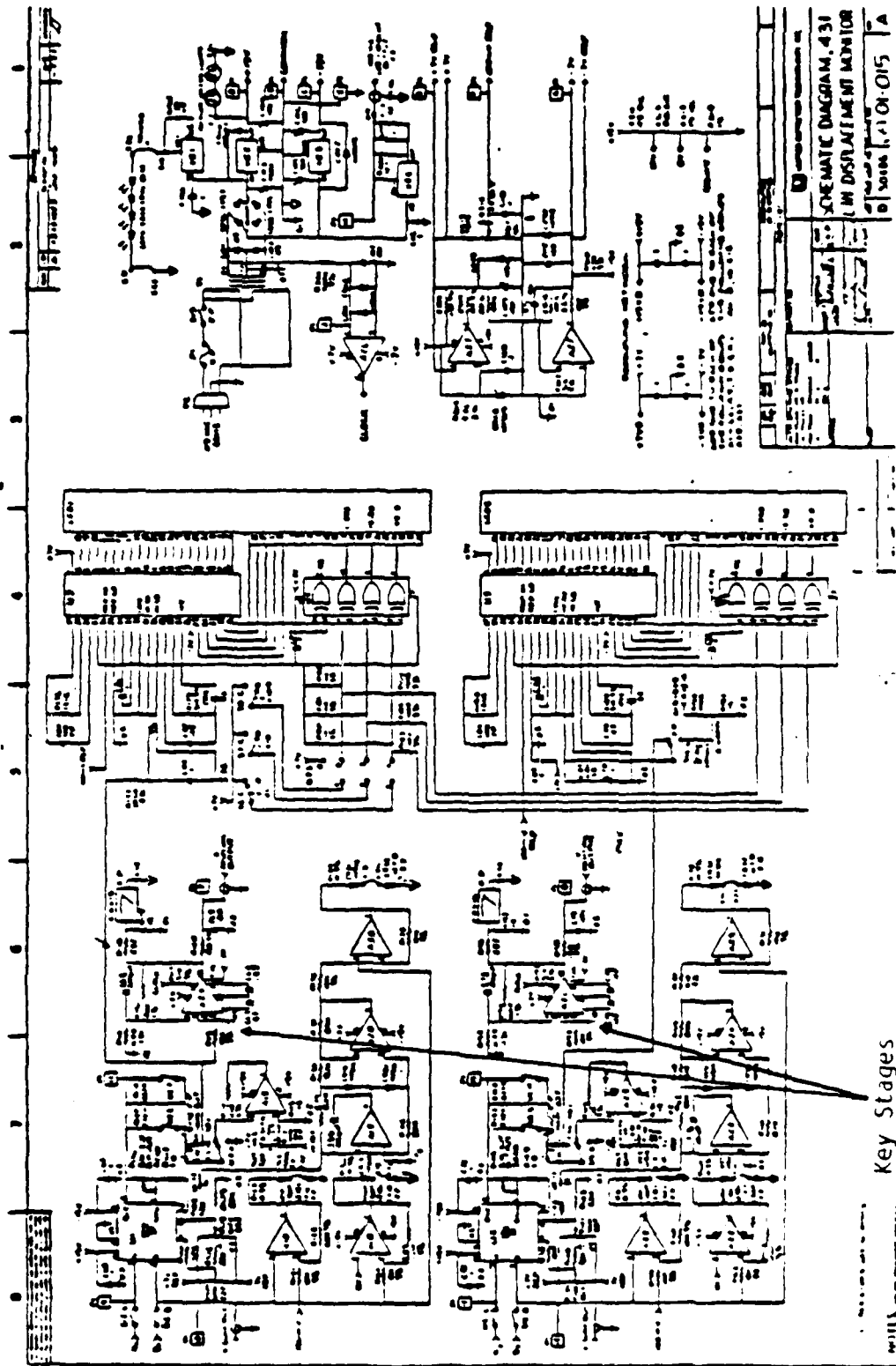


Figure 16b. UDT Schematic.

equations, gain is a function of displacement, spot size, intensity and detector area. As previously stated, the detector is 2.67mm square and the diameter of the beam striking the cell is 2.332mm. It has constant intensity. Then the gain can be strictly described by the displacement equations as long as the beam does not lap over the edges of the detector area. Although the tilt loop has the dynamic range to drive the beam off the detector area, this event is considered catastrophic and the result of an external disturbance. The gain of the UDT 431 corresponding to the entire beam in the right half plane (RHP) is 10 volts, and -10 volts for the entire beam in the left half plane (LHP). What was needed to model this behavior was an equation relating centroid displacement, and beam radius, to output gain. If the beam area is completely in the RHP, then the output gain can be modeled as:

$$\text{Gain} = \frac{10}{\pi r^2} (2A' - \pi r^2)$$

So now an equation is needed for A' . Using the approximation from Figure 17 and proceeding classically, A' can be represented as:

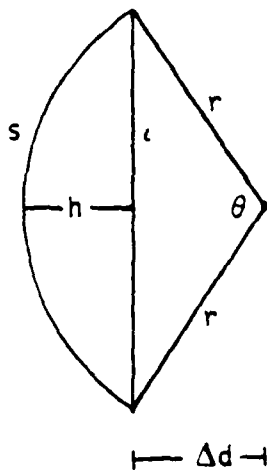
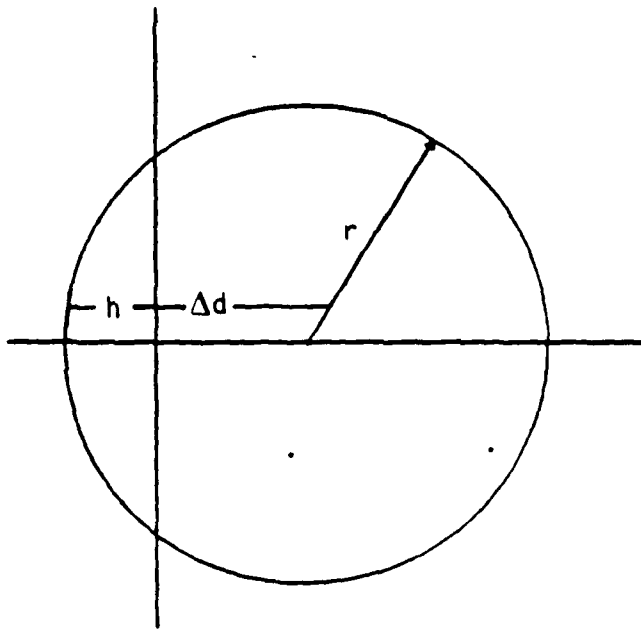
$$A' = \pi r^2 - \left[\frac{sr}{2} - 1(r-h) \right]$$

$$r-h = \Delta d$$

$$A' = \pi r^2 - \left[\frac{sr}{2} - 1\Delta d \right]$$

$$= \pi r^2 - \left[\frac{sr}{2} - 2|\Delta d| \sqrt{r^2 - \Delta d^2} \right]$$

$$A' = \pi r^2 - r^2 \cos^{-1} \frac{|\Delta d|}{r} + 2|\Delta d| \sqrt{r^2 - \Delta d^2}$$



$$\left(\frac{l}{2}\right)^2 = r^2 - \Delta d^2$$

$$l = 2\sqrt{r^2 - \Delta d^2}$$

$$\cos \frac{\theta}{2} = \frac{\Delta d}{r}$$

$$\theta = 2\cos^{-1} \frac{\Delta d}{r}$$

$$s = \theta r$$

$$s = 2r\cos^{-1} \frac{\Delta d}{r}$$

Figure 17. Quad Cell Gain Geometry.

Now combining this with the gain equation gives:

$$\text{Gain} = \frac{10\Delta d}{\pi r^2 |\Delta d|} (2\pi r^2 - 2r^2 \cos^{-1} \frac{|\Delta d|}{r} + 4|\Delta d| \sqrt{r^2 - \Delta d^2} - \pi r^2)$$

However, given that the entire beam remains on the detector area, the maximum Δx and Δy can be determined from comparing the beam diameter and detector size. It becomes apparent that a value greater than 0.169mm for Δx and Δy will displace the beam centroid such that a portion of the beam laps off the detector area. Therefore, Δx and Δy have a nominal range of plus or minus 0.169mm. Examining the behavior of this gain equation over this small nominal range, it was found that the following rectangular approximation was still more accurate. Let:

$$A' = 2r\Delta d + \frac{\pi r^2}{2} \quad \text{then,}$$

$$\text{Gain} = \frac{10}{\pi r^2} [2(2r\Delta d + \frac{\pi r^2}{2}) - \pi r^2] = \frac{40\Delta d}{\pi r}$$

So with the maximum Δx or $\Delta y = 0.169\text{mm}$ then the error is less than $4.4\text{e-}9$ square meters or the relative error is less than 0.174%.⁵

This figure is quite acceptable and this approximation is nicely linear. The overall transfer function for the quad cell is then:

$$\frac{8.0425\text{e}7 \frac{\Delta d K}{r}}{(s + 6.2832)(s + 10.0531)}$$

where K is a loop sensitivity factor of 0.1.

2.2 PISTON LOOP

The piston loop was modeled in six components and is shown in Figure 18. The deviation with respect to the reference position is modeled by a single input and single output model. There are also three piston loops in the model, two controlling a single aperture in piston and a third serving as a reference. The component models from the HVA and actuator are identical to those used in the tilt loop.

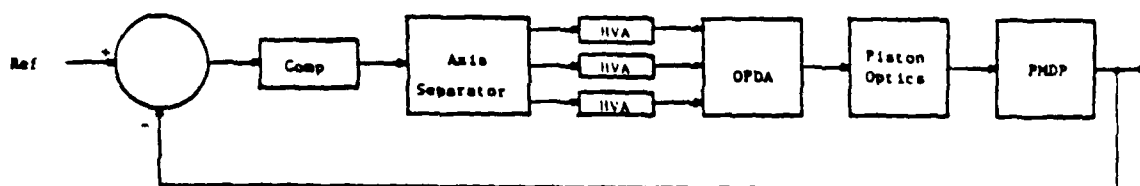


Figure 18. Piston Loop Block Diagram.

2.2.1 COMPENSATOR

The piston loop compensator differs from the tilt loop compensator only by a gain factor of 0.2. This was necessary to step down the gain from the phase management data processor to plus or minus one volt for the axis separator.

2.2.2 AXIS SEPARATOR

In the piston loop the axis separator model is very similar in function to the tilt loop model, except that here it must only interpret the movement commands for one input. A simple translation

matrix will translate a piston movement command into individual PZT displacement commands.

$$\begin{bmatrix} d1 \\ d2 \\ d3 \end{bmatrix} = 2.5 \begin{bmatrix} 1 \\ 1 \\ 1 \end{bmatrix} p$$

2.2.3 PISTON OPTICS

As previously stated, the optical transmission characteristics are outside the scope of this effort, but could be combined with this model if a joint study is desired. Here the behavior modeled was the translation of a given displacement from the actuator into an optical path difference (OPD). This transfer function is a function of the weighted average of the six different wavelengths lasing in the experiment; here, $\lambda = 0.5$ microns. It can be seen in Figure 19 that this transfer function is periodic every 2λ . The nominal operating range, save a gross external disturbance, is between -0.5 microns OPD and $+0.5$ microns OPD. Therefore the transfer function is simply -1.0 within the nominal operating range.

2.2.4 PHASE MANAGEMENT DATA PROCESSOR

The phase management data processor (PMDP) was built for this experiment by the BDM Corporation.¹² It is composed of three major subsystems: A Fairchild CCD 1300 Line Scan Camera (LSC), and camera control circuitry; analog-to-digital converter (ADC); computer processor. The aperture's beam is interfered with the reference beam and the resulting interferogram light pattern is focused on the charge

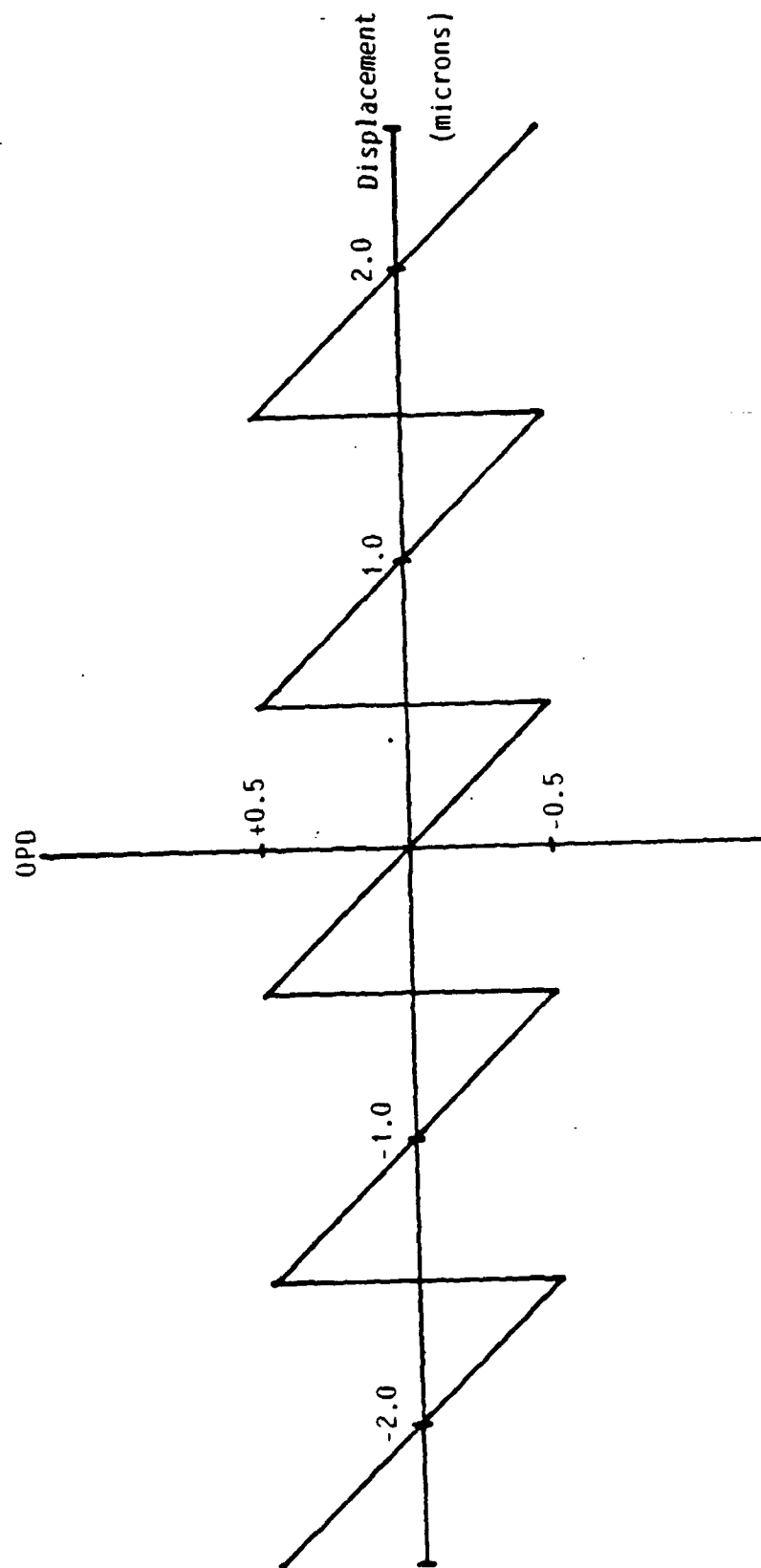


Figure 19. Displacement to OPD Translation.

coupled device (CCD). This interferogram is sampled every millisecond, passed through the ADC, and is represented as a linear array of 256 pixels with nine bits per pixel. Figure 20 shows an interferogram that has been imaged onto the LSC. This plot was made by outputting a single frame of digital data from the PMDP. The central portion of the digitized pattern is used for estimating the OPD between the two beams.² The algorithm for a linear measure of OPD is:

$$OPD = \frac{\int R - \int L}{\int R + \int L}$$

where R is the right side-lobe and L is the left side-lobe. This algorithm compares the integrated intensity of the two adjacent side lobes and normalizes the quantity by their sum. Simulated results of this algorithm are plotted in Figure 22. Under computer control the actuator was moved a given step size while taking data from the LSC and with the PMDP calculating the OPD values. Figure 21 was produced from this data. The widening of the plot toward the right side was caused by the nonlinearity of the old HVAs. Because of the 2π ambiguity, it is not possible with this algorithm to know when the two path lengths are exactly equal, corresponding to zero fringe. A global algorithm is used to determine zero fringe while the system is in open-loop. This linear algorithm is then used for closed-loop control. The modeling of this behavior was divided into two parts. The optical translation of displacement into OPD was used to develop a transfer function for the optics in the piston loop (see

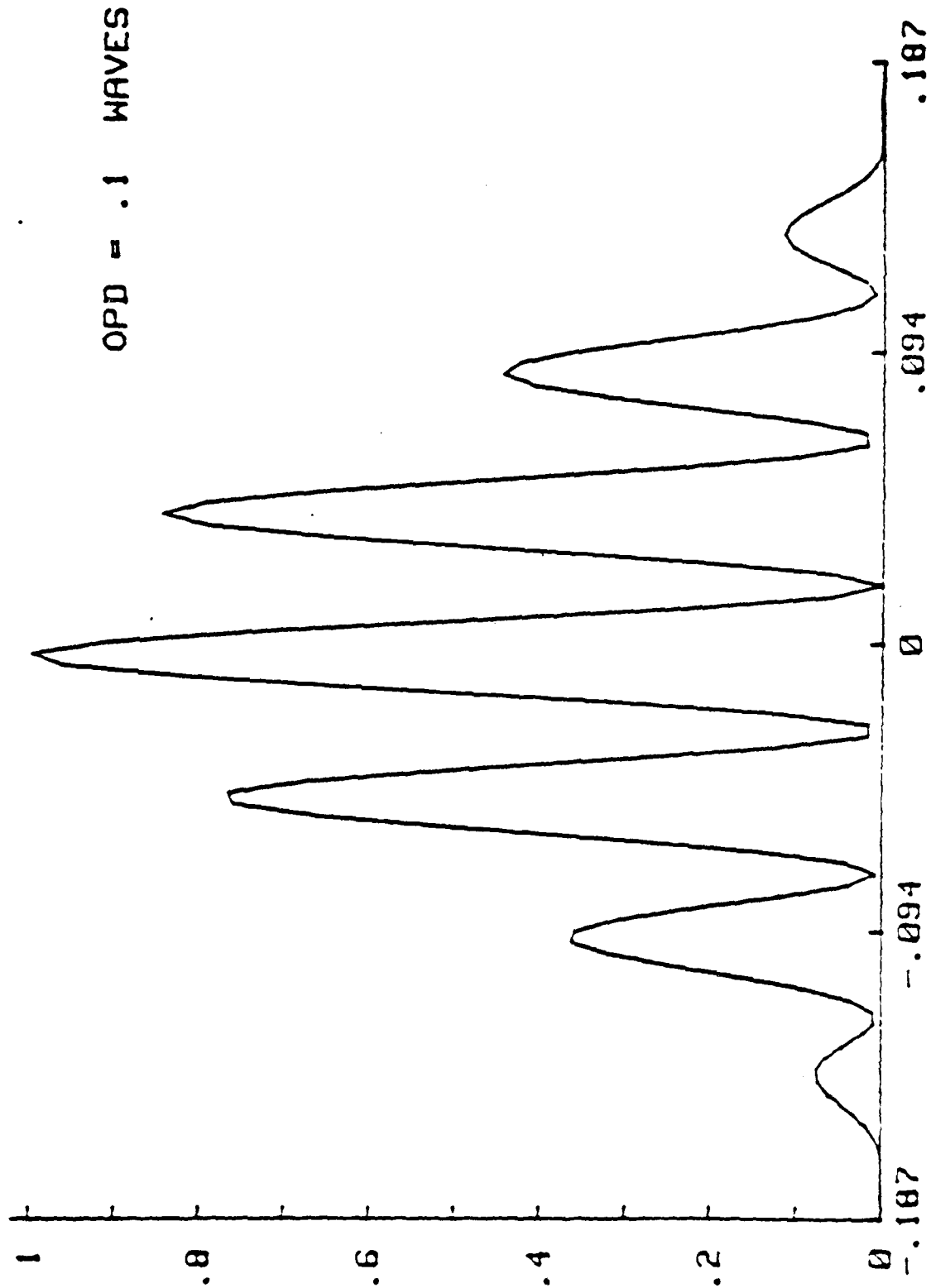


Figure 20. Interferogram Imaged onto LSC.

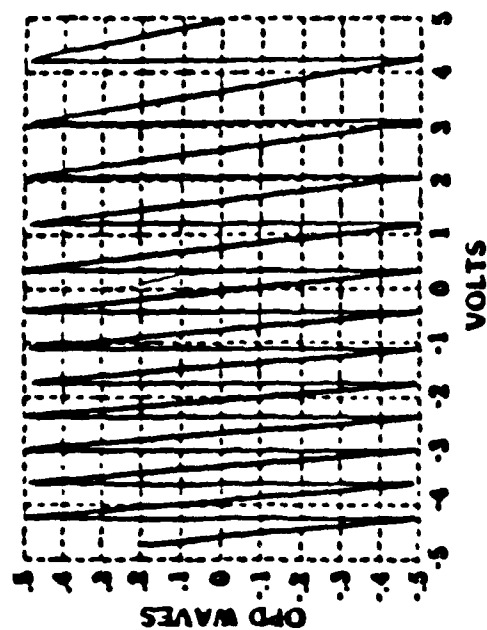


Figure 21.

Experimental Results.

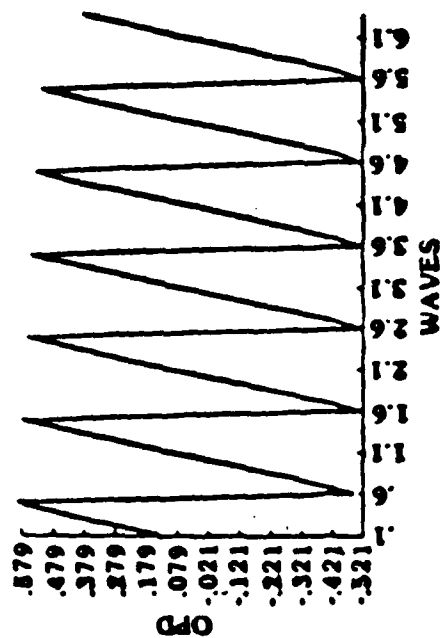


Figure 22.

Simulated Algorithm Results.

Section 2.2.3). OPD is then the input to the PMDP, with a gain in volts to correct to zero OPD as the output. Figure 23 illustrates this function of PMDP gain. To model the one millisecond delay, an e^{-Ts} term proceeds the transfer function for the PMDP. A zero-order hold is included to form a piecewise continuous output signal, and therefore, a $(1-e^{-Ts})/s$ term is cascaded onto the transfer function. In both instances, $T = 0.001$ seconds.

2.3 TILT-PISTON COUPLING

Referring again to Figure 2, there are two coupling mechanisms that potentially interweave the piston and tilt loop of each aperture. These are descriptively called piston corrupting tilt (PCT) and tilt corrupting piston (TCP).³ PCT has been observed in this experiment but had little significance as it was 30db down from the uncoupled tilt signal. TCP is potentially significant because it could corrupt the piston reference and thus couple together the three apertures. However, during the operation of this experiment, the magnitude of this coupling was never significant enough to allow measurement. So coupling in this model will be variable in magnitude, but whose significance will be along the magnitude previously stated.

During the alignment phase of the experiment, the axis separator is adjusted via the gain pots and summers such that the cross coupling signals are at least 30db down from the desired signal. This can be heuristically seen as aligning the misalignment angle so that the cross coupling between individual apertures is insignificant.

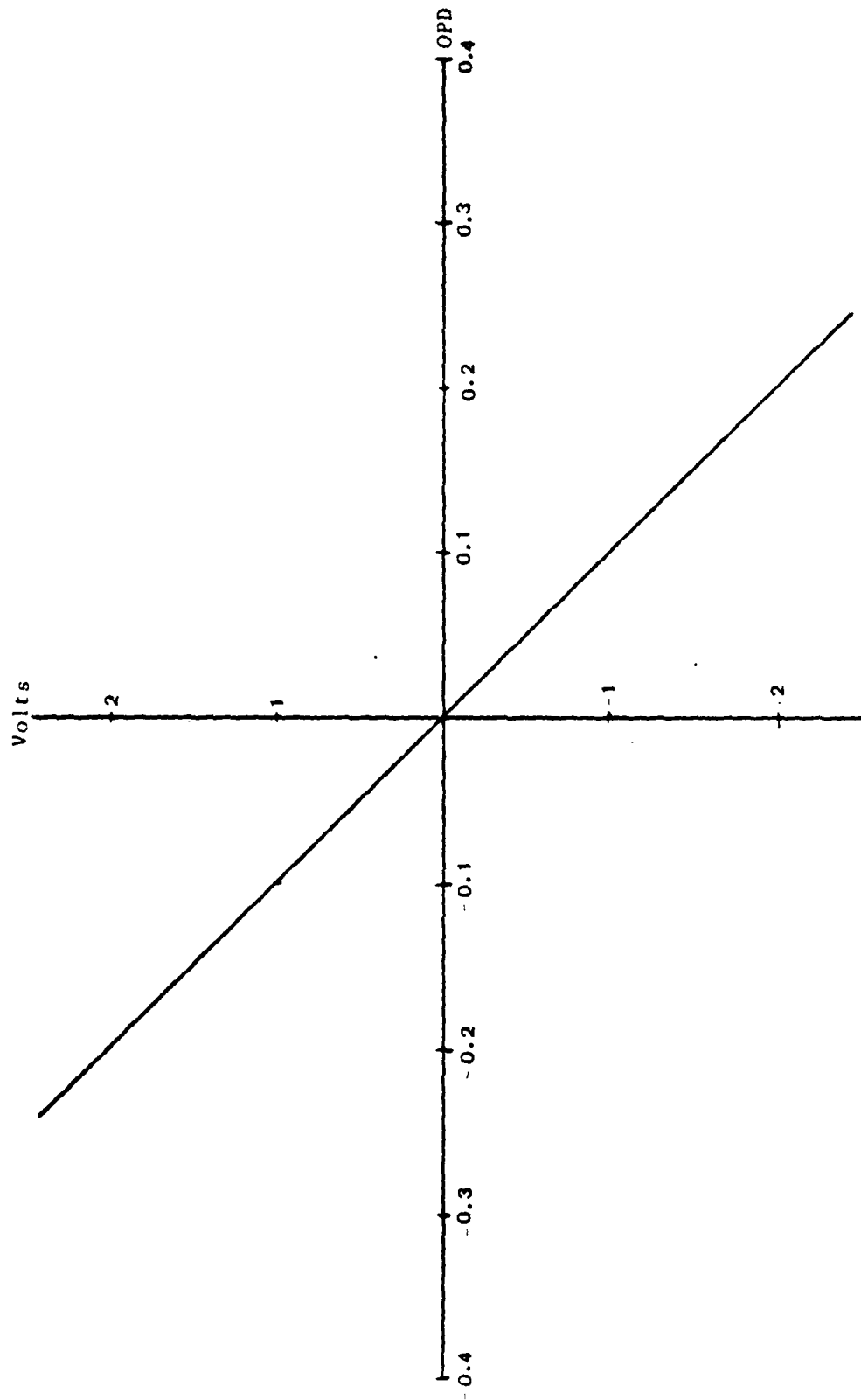


Figure 23. PMDP Gain.

CHAPTER 3

REALIZATION

The next step in the modeling scheme is to develop dynamical equations from the transfer-function matrices. For every realizable transfer-function matrix there is an unlimited number of dynamical-equation realizations. Therefore a major consideration in the realization process is to find a "good" realization. Here a realization that was both controllable and observable was pursued.⁷

3.1 TILT LOOP

Combining the component models, in cascade, from the previous chapter a forward-loop transfer-function (FLTF) matrix was obtained. The matrix was unit scaled to Krad/sec to keep the coefficients manageable. This is shown in Figure 24. Referring back to Figure 2, a closed-loop transfer-function (CLTF) matrix with unity feedback was computed and is shown in Figure 25. The CLTF matrix was transformed into an observable canonical form. The modal matrix corresponding to this system was badly conditioned and precluded many realization approaches. It was determined that a high-order, reducible realization would suffice. This realization form is a decoupled composite dynamical equation⁷ and is illustrated in Figure 26. The realization can be easily accomplished by inspection, but a penalty is incurred. This realization is not internally coupled and the

$$\begin{vmatrix} a_{11}(s) & a_{12}(s) \\ a_{21}(s) & a_{22}(s) \end{vmatrix}$$

$$g(s)$$

$$a_{11}(s) = 2.6898e9s^4 + 4.2251e10s^3 + 3.3184e11s^2 + 2.8148e12s + 1.1938e13$$

$$a_{12}(s) = 1.3786e9s^4 + 2.1655e10s^3 + 1.7008e11s^2 + 1.4427e12s + 6.1186e12$$

$$a_{21}(s) = -2.3334e7s^4 - 3.6652e8s^3 - 2.8787e9s^2 - 2.4419e10s - 1.0356e11$$

$$a_{22}(s) = 2.3418e9s^4 + 3.6785e10s^3 + 2.8891e11s^2 + 2.4507e12s + 1.0393e13$$

$$g(s) = s^{15} + 8.6314e1s^{14} + 3.5499e3s^{13} + 9.3401e4s^{12} + 1.7685e6s^{11} + 2.5561e7s^{10}$$

$$+ 2.9089e8s^9 + 2.6462e9s^8 + 1.9317e10s^7 + 1.1243e11s^6 + 5.1245e11s^5$$

$$+ 1.7688e12s^4 + 4.3548e12s^3 + 6.8123e12s^2 + 5.0766e12s$$

Figure 24. FLIF Tilt Loop.

$$\begin{vmatrix} \frac{a_{11}(s)}{g_{11}(s)} & \frac{a_{12}(s)}{g_{12}(s)} \\ \frac{a_{21}(s)}{g_{21}(s)} & \frac{a_{22}(s)}{g_{22}(s)} \end{vmatrix}$$

with $a_{ij}(s)$ defined in Figure 24.

$$\begin{aligned} g_{11}(s) = & s^{15} + 8.6314e1s^{14} + 3.5499e3s^{13} + 9.3401e4s^{12} + 1.7685e6s^{11} + 2.5561e7s^{10} \\ & + 2.9089e8s^9 + 2.6462e9s^8 + 1.9317e10s^7 + 1.1243e11s^6 + 5.1245e11s^5 \\ & + 1.7715e12s^4 + 4.3971e12s^3 + 7.1441e12s^2 + 7.8914e12s + 1.1938e13 \end{aligned}$$

$$\begin{aligned} g_{12}(s) = & s^{15} + 8.6314e1s^{14} + 3.5499e3s^{13} + 9.3401e4s^{12} + 1.7685e6s^{11} + 2.5561e7s^{10} \\ & + 2.9089e8s^9 + 2.6462e9s^8 + 1.9317e10s^7 + 1.1243e11s^6 + 5.1245e11s^5 \\ & + 1.7702e12s^4 + 4.3765e12s^3 + 6.9824e12s^2 + 6.5193e12s + 6.1186e12 \end{aligned}$$

$$\begin{aligned} g_{21}(s) = & s^{15} + 8.6314e1s^{14} + 3.5499e3s^{13} + 9.3401e4s^{12} + 1.7685e6s^{11} + 2.5561e7s^{10} \\ & + 2.9089e8s^9 + 2.6462e9s^8 + 1.9317e10s^7 + 1.1243e11s^6 + 5.1245e11s^5 \\ & + 1.7688e12s^4 + 4.3544e12s^3 + 6.8094e12s^2 + 5.0522e12s - 1.0356e11 \end{aligned}$$

$$\begin{aligned} g_{22}(s) = & s^{15} + 8.6314e1s^{14} + 3.5499e3s^{13} + 9.3401e4s^{12} + 1.7685e6s^{11} + 2.5561e7s^{10} \\ & + 2.9089e8s^9 + 2.6462e9s^8 + 1.9317e10s^7 + 1.1243e11s^6 + 5.1245e11s^5 \\ & + 1.7711e12s^4 + 4.3916e12s^3 + 7.1012e12s^2 + 7.5273e12s + 1.0393e13 \end{aligned}$$

Figure 25. CLTF Tilt Loop.

$$\begin{array}{c}
 \begin{array}{|c|} \hline \mathbf{B}_{11} \\ \hline \end{array} = \begin{array}{|c|} \hline \begin{array}{l} 1.1938e13 \\ 2.8148e12 \\ 3.3184e11 \\ 4.2251e10 \\ 2.6898e9 \end{array} \\ \hline \end{array} \quad \begin{array}{|c|} \hline \mathbf{B}_{12} \\ \hline \end{array} = \begin{array}{|c|} \hline \begin{array}{l} 6.1186e12 \\ 1.4427e12 \\ 1.7008e11 \\ 2.1655e10 \\ 1.3786e9 \end{array} \\ \hline \end{array} \quad \begin{array}{|c|} \hline \mathbf{B}_{21} \\ \hline \end{array} = \begin{array}{|c|} \hline \begin{array}{l} -1.0356e11 \\ -2.4419e10 \\ -2.8787e9 \\ -3.6652e8 \\ -2.3333e7 \end{array} \\ \hline \end{array} \quad \begin{array}{|c|} \hline \mathbf{B}_{22} \\ \hline \end{array} = \begin{array}{|c|} \hline \begin{array}{l} -1.0356e11 \\ 2.4507e12 \\ 2.8891e11 \\ 3.6785e10 \\ 2.3418e9 \end{array} \\ \hline \end{array}
 \end{array}$$

$$\mathbf{C}_1^T = \mathbf{C}_1^T - \mathbf{C}_1^T \mathbf{B}_{11}^{-1} \mathbf{B}_{12} \quad \mathbf{C}_2^T = \mathbf{C}_2^T - \mathbf{C}_2^T \mathbf{B}_{21} \mathbf{B}_{11}^{-1} \mathbf{B}_{12}$$

$$\begin{array}{|c|} \hline \mathbf{x}_{11} \\ \hline \end{array} = \begin{array}{|c|} \hline \begin{array}{l} \mathbf{A}_{11} \quad 0 \quad 0 \quad 0 \\ 0 \quad \mathbf{A}_{12} \quad 0 \quad 0 \\ 0 \quad 0 \quad \mathbf{A}_{21} \quad 0 \\ 0 \quad 0 \quad 0 \quad \mathbf{A}_{22} \end{array} \\ \hline \end{array} \quad \begin{array}{|c|} \hline \mathbf{x}_{12} \\ \hline \end{array} = \begin{array}{|c|} \hline \begin{array}{l} \mathbf{B}_{11} \quad 0 \\ 0 \quad \mathbf{B}_{12} \\ \mathbf{B}_{21} \quad 0 \\ 0 \quad \mathbf{B}_{22} \end{array} \\ \hline \end{array} \quad \begin{array}{|c|} \hline \mathbf{y}_1 \\ \hline \end{array} = \begin{array}{|c|} \hline \begin{array}{l} \mathbf{C}_{11} \quad \mathbf{C}_{12} \quad 0 \quad 0 \\ 0 \quad 0 \quad \mathbf{C}_{21} \quad \mathbf{C}_{22} \end{array} \\ \hline \end{array} \quad \begin{array}{|c|} \hline \mathbf{y}_2 \\ \hline \end{array} = \begin{array}{|c|} \hline \begin{array}{l} \mathbf{x}_{11} \\ \mathbf{x}_{12} \\ \mathbf{x}_{21} \\ \mathbf{x}_{22} \end{array} \\ \hline \end{array}$$

$$\mathbf{x}_T = \mathbf{A}_T^T \mathbf{x} + \mathbf{B}_T^T \mathbf{u} + \mathbf{y}_T = \mathbf{C}_T^T \mathbf{x}$$

Figure 26b. Tilt Loop Realization.

dimension is undesirably large. Model reduction will be an important follow-on issue. The "CONTROL.lab" computer package, made available through the Laboratory for Computer-aided Design of Systems and Robotics, was used extensively during this process and proved itself invaluable.¹⁸

3.2 PISTON LOOP

Combining the component models, in cascade, from the previous chapter a FLTF was obtained. It was again unit scaled to Krad/sec to remain consistent with the tilt loop, and to keep the coefficients manageable. This is shown in Figure 27. Referring back to Figure 2, a CLTF with unity feedback was computed and is shown in Figure 28. A realization was obtained by solving the 14th order differential equation for the highest derivative term. It was then transformed into a nested sequence of integrations. From this form a simulation diagram was drawn and the state differential equations obtained (see Figure 29). This procedure leads to an irreducible, observable canonical form realization.¹ This is shown in Figure 30.

3.3 STABILITY

The experimenters were particularly interested in the stability of the model, since this was a system attribute that they were exposed to in their daily experimental work. The tilt loop was chosen for closer examination because of greater experimenter familiarity and the relative ease of inspection. A pole-plot of the FLTF is illustrated

$$\begin{aligned}
& (e^{-0.001s} - e^{-0.002s})(1.8109e7s^4 + 2.8446e8s^3 + 2.2341e9s^2 + 1.8951e10s + 8.0371e10) \\
& \frac{s^{14} + 6.8977e1s^{13} + 2.3073e3s^{12} + 4.9974e4s^{11} + 7.8262e5s^{10} + 9.3213e6s^9 + 8.6381e7s^8 + 6.2642e8s^7}{+ 3.5215e9s^6 + 1.4929e10s^5 + 4.5153e10s^4 + 8.7063e10s^3 + 8.0370e10s^2}
\end{aligned}$$

Figure 27. FLIF Piston Loop.

$$\begin{aligned}
& (e^{-0.001s} - e^{-0.002s})(1.8109e7s^4 + 2.8446e8s^3 + 2.2341e9s^2 + 1.8951e10s + 8.0371e10) \\
& \frac{s^{14} + 6.8977e1s^{13} + 2.3073e3s^{12} + 4.9974e4s^{11} + 7.8262e5s^{10} + 9.3213e6s^9 + 8.6381e7s^8 + 6.2642e8s^7}{+ 3.5215e9s^6 + 1.4929e10s^5 + 4.5153e10s^4 + 8.7063e10s^3 + 8.0370e10s^2} \\
& + (e^{-0.001s} - e^{-0.002s})(1.8109e7s^4 + 2.8446e8s^3 + 2.2341e9s^2 + 1.8951e10s + 8.0371e10)
\end{aligned}$$

Figure 28. CLIF Piston Loop.

$$\frac{Y}{U} = \frac{(B_0 s^4 + B_1 s^3 + \dots + B_4)(e^{-r_1 s} - e^{-r_2 s})}{s^{14} + a_1 s^{13} + \dots + a_{12} s^2 + (e^{-r_1 s} - e^{-r_2 s})(B_0 s^4 + \dots + B_4)}$$

$$\stackrel{(4)}{B_0} u(t-r_1) + \stackrel{(3)}{B_1} u(t-r_1) + \dots - B_4 u(t-r_2) = \stackrel{(14)}{y(t)} + \stackrel{(13)}{a_1} y(t) + \dots - B_4 y(t-r_2)$$

$$\stackrel{(14)}{y(t)} = \stackrel{(4)}{B_0} u(t-r_1) + \stackrel{(3)}{B_1} u(t-r_1) + \dots - B_4 u(t-r_2) - \stackrel{(13)}{a_1} y(t) - \dots + B_4 y(t-r_2)$$

$$y(t) = \stackrel{(10)}{B_0} \int u(t-r_1) + \stackrel{(11)}{B_1} \int u(t-r_1) + \dots - B_4 \int u(t-r_2) - \stackrel{(14)}{a_1} y(t) - \dots + B_4 \int y(t-r_2) \stackrel{(14)}{y(t)}$$

$$y(t) = -\stackrel{(2)}{a_1} \int y(t) - \stackrel{(9)}{a_2} \int y(t) - \dots - \stackrel{(9)}{a_9} \int y(t) + \int (-\stackrel{(10)}{a_{10}} y(t) + \stackrel{(10)}{B_0} u(t-r_1) \dots$$

$$y(t) = \int (-\stackrel{(2)}{a_1} y(t) + \int (-\stackrel{(2)}{a_2} y(t) + \dots + \int (-\stackrel{(9)}{a_9} y(t) + \int (\dots)) \dots) dt$$

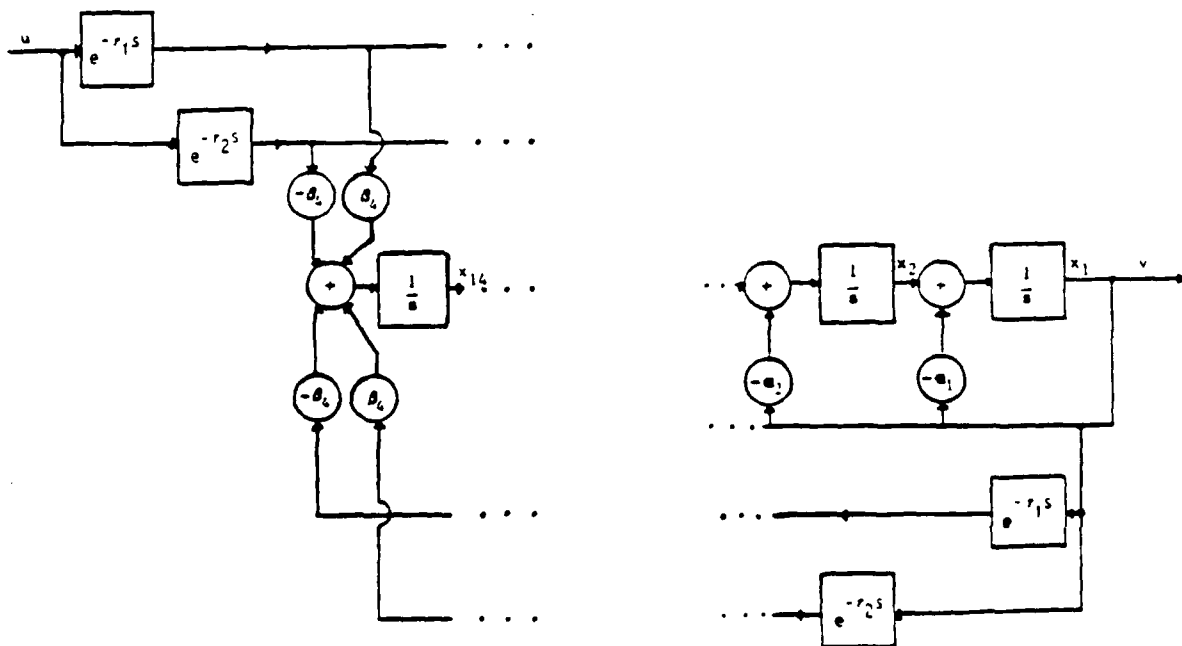


Figure 29. Piston Loop Realization Procedure.

in Figure 31; the poles are tabulated in Table 1. The pole at the origin represents the integrator contained within the compensator. A pole-plot of the corresponding CLTF matrix is shown in Figure 32, with poles tabulated in Table 2. Both of these plots were broadly accepted by the experimenters as representative of known system behavior. The marginally RHP poles in the CLTF pole-plot correspond to the constant coefficients in terms g_{11} , g_{21} , and g_{22} from the CLTF matrix. The experimenters claim that this instability does indeed exist prior to open-loop adjustments made at the onset of an experimental run.

3.4 LARGE-SCALE SYSTEM

The combined, three-aperture model that corresponds to Figure 2 consists of three tilt loops and two piston loops. A realization of this 208th order system is shown in Figure 33 using the tilt and piston loop matrix partitions defined in Figures 26 and 30 respectively. It is apparent that this system is coupled only through the functions, f and ϵ . As was stated earlier, although the exact mathematical characteristics of these functions are not known, their general dynamics are bounded above by a constant M , where M is 30db down in magnitude from the pure signal. The magnitude of ϵ is still smaller, and has never been significant enough to facilitate measurement.

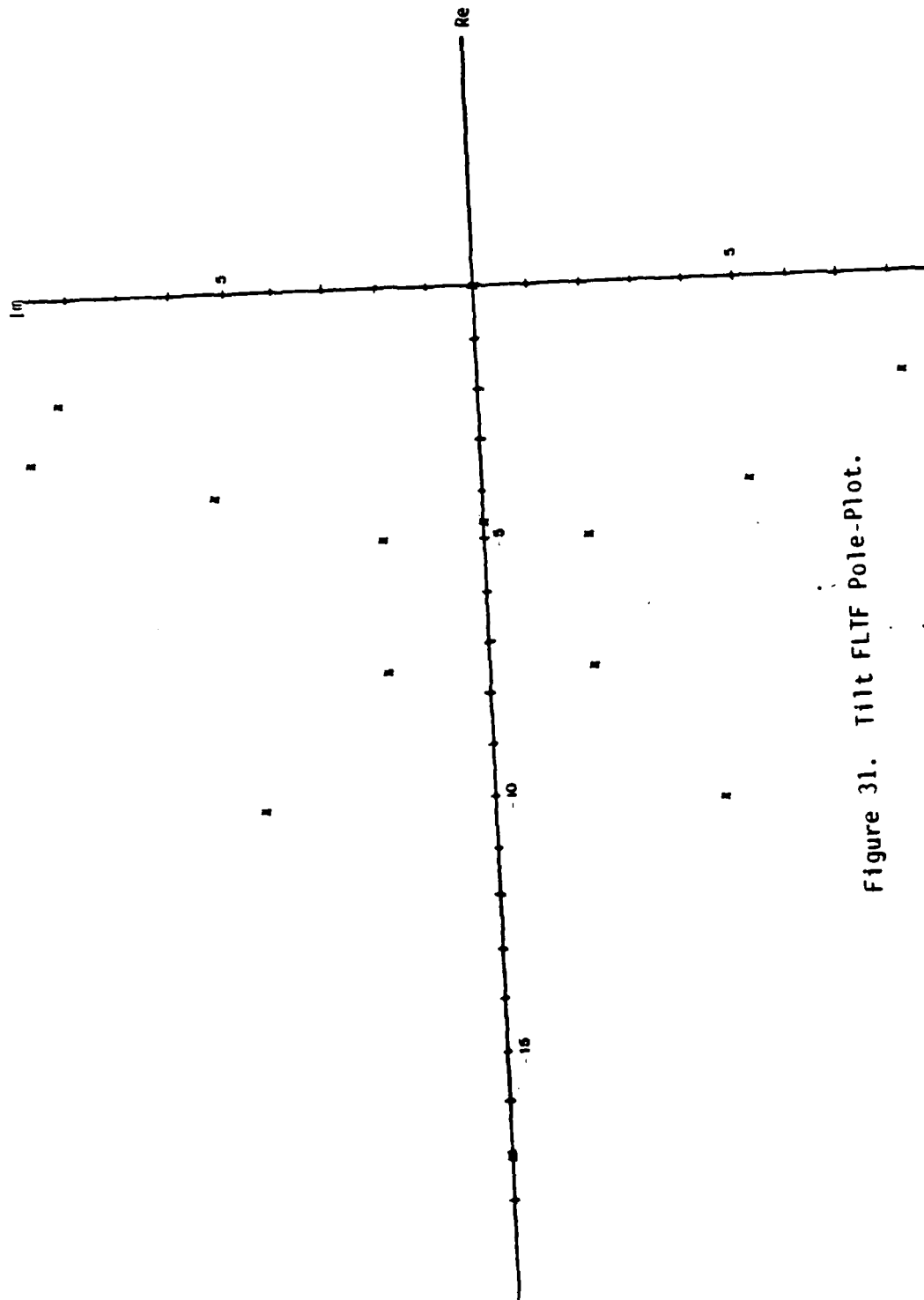


Figure 31. Tilt FLIF Pole-Plot.

Table 1.
Tilt FLTF Poles.

<u>Real Part</u>	<u>Imaginary Part</u>
+ 0.0000	+ 0.0000
- 2.1409	- 8.2564
- 2.1409	+ 8.2564
- 3.1957	- 8.8213
- 3.1957	+ 8.8213
- 3.9953	- 5.2116
- 3.9953	+ 5.2116
- 4.6890	- 0.0000
- 5.0922	- 1.9196
- 5.0922	+ 1.9196
- 7.6346	- 1.9715
- 7.6346	+ 1.9715
- 10.2077	- 4.5132
- 10.2077	+ 4.5132
- 17.0922	+ 0.0000

Table 2.
Tilt CLTF Matrix Poles.

A_{11} Poles		A_{12} Poles	
Real Part	Imaginary Part	Real Part	Imaginary Part
+ 0.2486	- 1.5939	- 0.1451	- 1.3085
+ 0.2486	+ 1.5939	- 0.1451	+ 1.3085
- 1.9016	- 6.0063	- 2.0866	- 8.4889
- 1.9016	+ 6.0063	- 2.0866	+ 8.4889
- 2.0050	- 8.6034	- 2.3657	- 5.8272
- 2.0050	+ 8.6034	- 2.3657	+ 5.8272
- 3.7082	- 8.9987	- 3.5295	- 8.8611
- 3.7082	+ 8.9987	- 3.5295	+ 8.8611
- 7.9799	- 0.6418	- 7.8557	- 0.8963
- 7.9799	+ 0.6418	- 7.8557	+ 0.8963
- 8.2251	- 6.0505	- 7.9842	- 5.4214
- 8.2251	+ 6.0505	- 7.9842	+ 5.4214
- 11.0270	- 3.8851	- 10.6374	- 3.9681
- 11.0270	+ 3.8851	- 10.6374	+ 3.9681
- 17.1175	- 0.0000	- 17.1057	- 0.0000

A_{21} Poles		A_{22} Poles	
Real Part	Imaginary Part	Real Part	Imaginary Part
+ 0.2000	+ 0.0000	+ 0.1648	- 1.5396
- 2.1454	- 8.2588	+ 0.1648	+ 1.5396
- 2.1454	+ 8.2588	- 2.0040	- 5.9663
- 3.1923	- 8.8154	- 2.0040	+ 5.9663
- 3.1923	+ 8.8154	- 2.0260	- 8.5711
- 4.0693	- 5.2807	- 2.0260	+ 8.5711
- 4.0693	+ 5.2807	- 3.6599	- 8.9634
- 4.3571	- 2.2317	- 3.6599	+ 8.9634
- 4.3571	+ 2.2317	- 7.8596	- 0.0000
- 4.9494	+ 0.0000	- 8.1316	- 5.9340
- 8.2201	- 2.3058	- 8.1316	+ 5.9340
- 8.2201	+ 2.3058	- 8.1936	+ 0.0000
- 10.1617	- 4.5045	- 10.9172	- 3.9844
- 10.1617	+ 4.5045	- 10.9172	+ 3.9844
- 17.0927	+ 0.0000	- 17.1130	+ 0.0000

CHAPTER 4

CONCLUSIONS

A large-scale realization of this experimental system has been obtained. This model incorporates the potential for complete coupling between tilt and piston loops of the same aperture, although all data indicates that the system is weakly coupled. As with most projects of this type, as many questions have been raised as conclusions drawn. Further examination of the coupling could be particularly interesting, and applied to other multiple aperture systems with similar attributes. Individual component models could be extended, or used in their present form, for use in other system modeling efforts. The combination of this model with the separate system optical characterization could be most illuminating. This model represents a valuable investigative tool for the experimenters to explore various control issues such as increased system bandwidth, and near-optimum control. The development of more robust control algorithms, that would continue to provide asymptotic stability and regulation under perturbation of plant parameters, could also be explored. A priori information could also be obtained regarding a potential hardware component upgrade. The model could be expanded to include the DC drift tracker leg to more completely duplicate the entire PHASAR

experiment, or extended and generalized for use as a design tool for multiple aperture systems.

This work also represents a point of departure for additional issues that could warrant further study. A full-scale computer simulation would decisively verify the modeling of this system and would provide a computational aid for the experimenters. The simulation should be accomplished with inputs set to zero, and driven only by a disturbance injected into the quad cell and PMDP. This disturbance rejection simulation will most closely match experimental conditions. Model reduction would be of great value for a system this large in dimension. In particular, the reduction of the tilt loop to a more manageable order would significantly reduce the complete model's order. There are a number of model reduction schemes that could be applied to this system; the balanced method appears particularly attractive.¹⁴ This approach uses concepts of controllability and observability to determine a reduced-order model. The full-order model has many unobservable or uncontrollable modes, and is therefore an appropriate candidate for this method. Near-optimum control techniques could be applied,¹⁰ and the system decomposed via interaction prediction²¹ to find a near-optimal hierarchical control regime. These efforts would further strengthen this model's utility.

APPENDIX

GLOSSARY OF ABBREVIATIONS

- ADC - Analog to Digital Converter - A signal converter that is a subsystem of the PMDP.
- CCD - Charge Coupled Device - An 1024 element photo sensor used as an image detector in the LSC subsystem of the PMDP.
- CLTF - Closed-Loop Transfer Function.
- FLTF - Forward-Loop Transfer Function.
- HVA - High Voltage Amplifier - A key component in the PHASAR experiment.
- LHP - Left Half Plane - Usually used in reference to the s-plane during stability considerations.
- LSC - Line Scan Camera - An electronic camera system that produces an analog video output waveform representing the spatial distribution of the time-integrated brightness across one scanned line of an optical image. A subsystem of the PMDP.
- OPD - Optical Path Difference - The difference in path length between two apertures.
- OPDA - Optical Path Difference Adjuster - A key component in the PHASAR experiment.
- PCT - Piston Corrupting Tilt - The phenomenon of commanded piston displacements inducing uncommanded tilt displacements.
- PHASAR - PHASed ARray experiment - The experiment of interest located at the Air Force Weapons Laboratory.
- PMDP - Phase Management Data Processor - A key component in the piston loop of the PHASAR experiment.
- PZT - PieZo-electric Transducer - The key dynamical element in the OPDA.
- RHP - Right Half Plane - Usually used in reference to the s-plane during stability considerations.
- TCP - Tilt Corrupting Piston - The phenomenon of commanded tilt displacements inducing uncommanded piston displacements.
- UDT - United Detector Technology - A position sensing photodetector manufacturer. Their equipment is a key component in the tilt loop of the PHASAR experiment.

REFERENCES

- ¹Brogan, W. L., 1985, Modern Control Theory, Prentice-Hall, Englewood Cliffs, NJ, pp. 233-241, 306, 320, 373-374.
- ²Butts, R. R., 1983, "Analysis of phase measurement algorithm using two-beam interference," SPIE Proceedings, 440, Synthetic Aperture Systems.
- ³Butts, R. R., 1983, "The effects of piston and tilt errors on the performance of multiple mirror telescopes," SPIE Proceedings, 440, Synthetic Aperture Systems.
- ⁴Butts, R. R., Cusumano, S. J., Fender, J. S., DeHainaut, C. P., 1983, "A concept for a phased array laser transmitter," SPIE Proceedings, 440, Synthetic Aperture Systems.
- ⁵Burden, R. L., Faires, J. D., Reynolds, A. C., 1978, Numerical Analysis, Prindle, Weber and Schmidt, Boston, pp. 10-11.
- ⁶Carreras, R. A., Cusumano, S. J., Andrews, M. G., Jordan, D. H., 1983, "Overview of a phased array experiment," SPIE Proceedings, 440, Synthetic Aperture Systems.
- ⁷Chen, C. T., 1984, Linear System Theory and Design, Holt, Rinehart and Winston, New York, pp. 157-161, 327-329.
- ⁸D'Azzo, J. J., Houpis, C. H., 1981, Linear Control System Analysis and Design, McGraw-Hill, New York, pp. 250-259.
- ⁹Fender, J. S., 1983, "Synthetic apertures: An overview," SPIE Proceedings, 440, Synthetic Aperture Systems.
- ¹⁰Jamshidi, M., 1983, Large-Scale Systems-Modeling and Control, North-Holland.
- ¹¹Johnson, C. L., 1963, Analog Computer Techniques, McGraw-Hill, pp. 21-37.
- ¹²Jordan, D. H., Morrow, D. R., Goranson, R. W., 1983, "Control loop sensor for an optical synthetic aperture," SPIE Proceedings, 440, Synthetic Aperture Systems.

- 13Marker, D. K., Coates, E. L., 1985, "Three degree of wide bandwidth optical path adjuster," SPIE Proceedings, 546, Synthetic Aperture Optical Systems.
- 14Moore, B. C., 1981, "Principal component analysis in linear systems: Controllability, observability, and model reduction," IEEE Trans. Automat. Contr., vol. AC-26, Feb. 1981.
- 15Kuo, B. C., 1975, Automatic Control Systems, Prentice-Hall, Englewood Cliffs, NJ, pp. 203-208.
- 16Ogata, K. 1970, Modern Control Engineering, Prentice-Hall, Englewood Cliffs, NJ, pp. 721-741.
- 17Ricci, F. J., 1972, Analog/Logic Computer Programming and Simulation, Spartan Books, New York, pp. 31-40.
- 18Schotik, G. L., Jamshidi, M., Yenn, T. C., 1985, CONTROLlab User's Guide - A CAD Language for Multivariable Control and Kalman Filtering, Technical Report, CAD Laboratory for Systems and Robotics, University of New Mexico Department of Electrical and Computer Engineering, LCAD-85-02.
- 19Shinners, S. M., 1978, Modern Control System Theory and Application, Addison-Wesley, Reading, MA, pp. 43-44.
- 20Suizo, R. I., Carreras, R. A., 1985, "Overview of optical control of a phased array experiment," SPIE Proceedings, 546, Synthetic Aperture Optical Systems.
- 21Takahara, Y., 1965, "A multi-level structure for a class of dynamical optimization problems," M.S. thesis, Case Western Reserve University, Cleveland, OH.
- 22Vidyasagar, M., 1978, Nonlinear System Analysis, Prentice-Hall, Englewood Cliffs, NJ, pp. 21-49.

END

1-87

DTIC